International Journal of Applied Earth Observation and Geoinformation 150 (2026) 105337

Contents lists available at ScienceDirect

International Journal of Applied Earth Observation and Geoinformation

journal homepage: www.elsevier.com/locate/jag

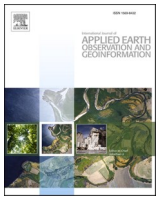

Continuous change monitoring of supraglacial lakes during melt and non-melt seasons with multi-source satellite imagery and deep learning

Dongyu Zhu [a,b,c], Chunxia Zhou [b,c,*], Xiaoli Chen [b,c], Jiani Ouyang [d], Ce Zhang [e,f]

[a] School of Mathematics and Computer Science, Wuhan Polytechnic University, Wuhan 430048 China
[b] Chinese Antarctic Center of Surveying and Mapping, Wuhan University, Wuhan 430079 China
[c] Key Laboratory of Polar Environment Monitoring and Public Governance (Wuhan University), Ministry of Education, Wuhan 430079 China
[d] School of Construction Engineering, Shenzhen Polytechnic University, Shenzhen 518055 China
[e] School of Geographical Sciences, University of Bristol, Bristol BS8 1SS, UK
[f] UK Centre for Ecology & Hydrology, Library Avenue, Lancaster LA1 4AP, UK

ARTICLE INFO

Keywords:
Supraglacial Lake
Multi-source remote sensing
Buried Lake
Deep learning
Greenland

ABSTRACT

The surface melting of ice sheets is gradually intensifying with rising global temperatures. Supraglacial lakes (SGLs), an essential component of the ice-surface hydrological system, are significant for the ice sheet mass balance. SGLs have been shown to persist year-round, with some lakes retaining as buried lakes within the ice sheet subsurface throughout the winter, rather than completely draining and freezing after the melt season. Accordingly, continuous change monitoring of SGLs during melt and non-melt seasons is crucial for understanding ice sheet storage and drainage processes. Herein, we used optical and SAR satellite data to monitor the SGLs variability in the southwest Greenland from 2020 to 2022. Three deep learning models, namely, U-Net, attention U-Net (AU-Net), and attention recurrent residual U-Net (AR2U-Net), are compared. AR2U-Net showed the optimal performance in SGL extraction in SAR images. However, SGLs are not precisely extracted from SAR images in areas with high water content due to the influence of wet snow, so optical imagery extraction results are referenced in the study of melting seasons. The results of the SGL changes from 2020 to 2022 indicated that, the changes in the SGL area between years are insignificant, and the main differences are attributed to extreme climatic events occurring in Greenland. Majority of the newly formed SGLs drained at the end of the melt season, with about 16.52% forming buried lakes, which are concentrated in the mid-high elevation. However, the storage of newly buried lakes is not sensitive to an intense melting season, with the new meltwater retained in comparable amounts at the end of the three melt seasons. Buried lakes that remained unopened throughout the year are typically found at elevated altitudes, and their areas is around 2–3 times that of the retained liquid water from the melt season. Overall, the extraction methods and analytical approaches used in this study, based on a longer time series and a wider study scope will aid the further discussion of the seasonal area changes in SGLs.

1. Introduction

Glaciers store approximately three-quarters of the Earth's fresh water resources. The Greenland ice sheet (GrIS), the second largest continental ice sheet in the world, holds an ice volume equivalent to a sea-level rise of 7.4 m (Morlighem et al., 2017). The ice sheet's hydrological system is a major component of the mass loss (Trusel et al., 2018). Studies have shown that the surface melting on the GrIS can enhance glacial sliding, particularly in areas with crevasses (Hoffman et al., 2018). The runoff that passes through supraglacial stream/river networks can develop form a drainage system that expels water toward the ice edge and global ocean (Smith et al., 2017). Supraglacial lakes (SGLs) play a crucial role in the hydrological system in ice sheets and constitute an important unit for the formation and storage of meltwater (Wendleder et al., 2021a). SGLs refer to ponds formed by rainfall and thermodynamic processes of glaciers, which converges in the depression of ice sheet. A large number of SGLs are present on the GrIS, and most of them are distributed in western and northeastern Greenland (Hu et al., 2022). The extent of the SGLs has further expanded with global warming and continues to advance inland (Zhu et al., 2022).

Remote sensing technology is extensively used in the monitoring of SGL changes, with a primary focus on capturing the significant changes

* Corresponding author at: Chinese Antarctic Center of Surveying and Mapping, Wuhan University, Wuhan 430079 China.
E-mail address: zhoucx@whu.edu.cn (C. Zhou).

https://doi.org/10.1016/j.jag.2026.105337
Received 27 January 2024; Received in revised form 30 April 2026; Accepted 9 May 2026
Available online 12 May 2026

of SGLs during the summer. However, SGLs can also maintain water through the winter as buried lakes (Zhu et al., 2023), which can expedite future lake formation and warm underlying ice even in winter (Law et al., 2020). Buried lakes are meltwater features that contain liquid water and exist under layers of snow, firn, and/or ice (Dunmire et al., 2021). Experiments have shown that these buried lakes also experience storage and drainage events during winter, and they serve a small year-round source of meltwater in the GrIS hydrologic system (Benedek and Willis, 2020). Although open water is easily identifiable in optical images during the melting summer, buried SGLs beneath snow remain unobservable in optical images during the non-melting season. Accordingly, the combined application of optical and synthetic aperture radar (SAR) satellites is frequently used to detect the development of SGLs during the year-round season (Dirscherl et al., 2022). However, the SAR imagery systematically failed to discriminate narrow lakes and lakes in corrugated topography (Johansson & Brown, 2012). Moreover, the backscatter coefficient of SAR imagery is highly susceptible to the water content of the snow surface (Buchelt et al., 2021), making it difficult to extract SGLs from SAR imagery during the melt season. Thus, optical and SAR satellites are inseparable in the investigation of the entire process (melting and non-melting seasons) of SGL development.

Research on SGL changes based on optical and SAR imagery is increasing. Johansson and Brown (2012) manually mapped the SGLs in west Greenland with a moderate resolution imaging spectroradiometer (MODIS) and ENVISAT SAR and affirmed the potential of SAR imagery for winter lake mapping. Miles et al. (2017) monitored the SGLs on the GrIS using Sentinel-1 SAR and Landsat-8 OLI imagery with a semi-automatic threshold method to detect fast and slow surface lake drainage events. Chouksey et al. (2021) completed the classification of glacier features in parts of central Dronning Maud Land, East Antarctica with support vector machine and supervised classification algorithm using Landsat-8, RISAT-1, and Sentinel-1 data. Zheng et al. (2023) used the self-adaptive thresholds for SAR to monitor the buried lake in GrIS of each winter during 2017–2022. Deep learning extraction of SGLs have gradually emerged as it is more suitable for batch processing and high-precision adaptive detection compared with traditional methods, such as Canny edge detection and texture monitoring (Dirscherl et al., 2022; Jiang et al., 2022).

Although a year-round time scale for SGLs' development research is vital, current studies divide the grown of SGLs in the melt and non-melt seasons. The integration of optical and SAR imagery is aimed at expanding the dataset for extracting information about SGLs during the melting season (Dirscherl et al., 2021b, 2021a; Leeson, 2020; Wendleder et al., 2021b) and the pre-determination of the location of the winter buried lakes (Benedek and Willis, 2020). Nevertheless, analysis of the SGL changes by splitting the melt and non-melt seasons does not provide a comprehensive understanding of buried lake development. Several studies covered the SGL changes during the melt and non-melt seasons. However, the experiments needed further improvement due to the limitations in research area, spatial resolution of satellite images, extraction methods, and melt extent (Jiang et al., 2022; Zheng et al., 2023).

We used Sentinel-1 SAR and Sentinel-2 optical imagery in 2020 to 2022 to identify SGLs across part of southwest GrIS, near Jakobshavn Isbræ. The satellite images were downloaded and pre-processed using the Google Earth Engine (GEE) platform. The extraction of SGLs from the optical images was performed using the normalized difference water index (NDWI). Three deep learning models (standard U-Net, attention U-Net [AU-Net], and attention recurrent residual U-Net [AR2U-Net]) are compared for SGL extraction from SAR images. This study includes SGL distribution at 12 time points during the melt and non-melt seasons. Moreover, we discuss the maximum water range during the melt season. The objectives include providing a new perspective of year-around SGL extraction combining optical and SAR imagery, and discussing SGL spatial changes over various time periods in a year, with emphasis on the transition between melting and non-melting seasons. The results of this study will facilitate the analysis of SGLs' area changes throughout the year and provide highly comprehensive data on developmental processes in SGLs on the ice sheet.

2. Data and materials

2.1. Study site

The study is conducted in the southwestern region of the GrIS, recognized as the most intense region for lakes and rapid drainage events, covering an area of approximately 27,800 km^2 (Fig. 1). The region has undergone extreme glacial activity, with a total mass loss exceeding 200 Gt from 1985 to 2017 (Felikson et al., 2017). This area comprises a rich surface hydrological system with extensive SGLs, stream/river networks, moulins, etc.

The study area was buffered 8 km inland from the ice sheet edge to minimize mis-extraction caused by seawater (Moussavi et al., 2020). This area was divided into 4244 grids with each sized 256*256 pixels at an elevation of approximately 1900 m, with every grid serving as the basic unit for deep learning.

2.2. Data sources

The all-weather Sentinel-1 (S1) radar and high-resolution Sentine-2 (S2) optical imagery are commonly used in SGL extraction (Spergel et al., 2021). We used S1 data acquired in interferometric wide swath (IW) mode with dual polarization (HH + HV) and Level-1 Ground Range Detected, along with top-of-atmosphere reflectance data of S2 to extract SGLs in different seasons. These data (10 m range resolution) were downloaded and pre-processed using the GEE platform (https://earthengine.google.com). Twelve time points from 2020 to 2022 were selected for the lake extraction in SAR. Meanwhile, each S2 image collection from May to October were used for the lake extraction during the melt season (Table 1). This study used S1 images from similar time points in February, May, August, and November of 2020, 2021, and 2022 as the foundation for extracting SGLs from SAR imagery.

The elevation data used in the experiments were derived from ArcticDEM at a 10 m resolution, with coverage numbers 20–38, 20–39, 19–38, 19–39, 19–40, 18–38, 18–39, 18–40, 17–38, 17–39, and 17–40. ArcticDEM is a pan-Arctic topography dataset derived from high-resolution stereo images and freely available from https://arcticdem.org.

3. Methods

3.1. Processing in GEE

This study utilized S1 and S2 imagery, with data download and preprocessing conducted on the GEE platform. The S1 SAR data in HH and HV were Lee sigma filtered (Mullissa et al., 2021) and topographically corrected in GEE. The S2 optical data were selected with cloud coverage less than 10%; these optical images were used to calculate the maximum water extent during the melt season (May to October) based on the normalized difference water index adapted for ice ($NDWI_{ice}$) (Yang & Smith, 2013). The maximum water extent obtained from optical imagery will be used for the initial identification of SGLs in the SAR imagery.

3.2. Sentinel-1 label production

Backscatter in SAR images is a consequence of diffuse backscattering from the surface and volume scattering from the subsurface, which is closely related to the dielectric properties and structures of the surface and subsurface (Tsai et al., 2019). Meanwhile, C-band S1 SAR data are sensitive to snowmelt and the local incidence angle relating to observation geometry and terrain (Liang et al., 2021).

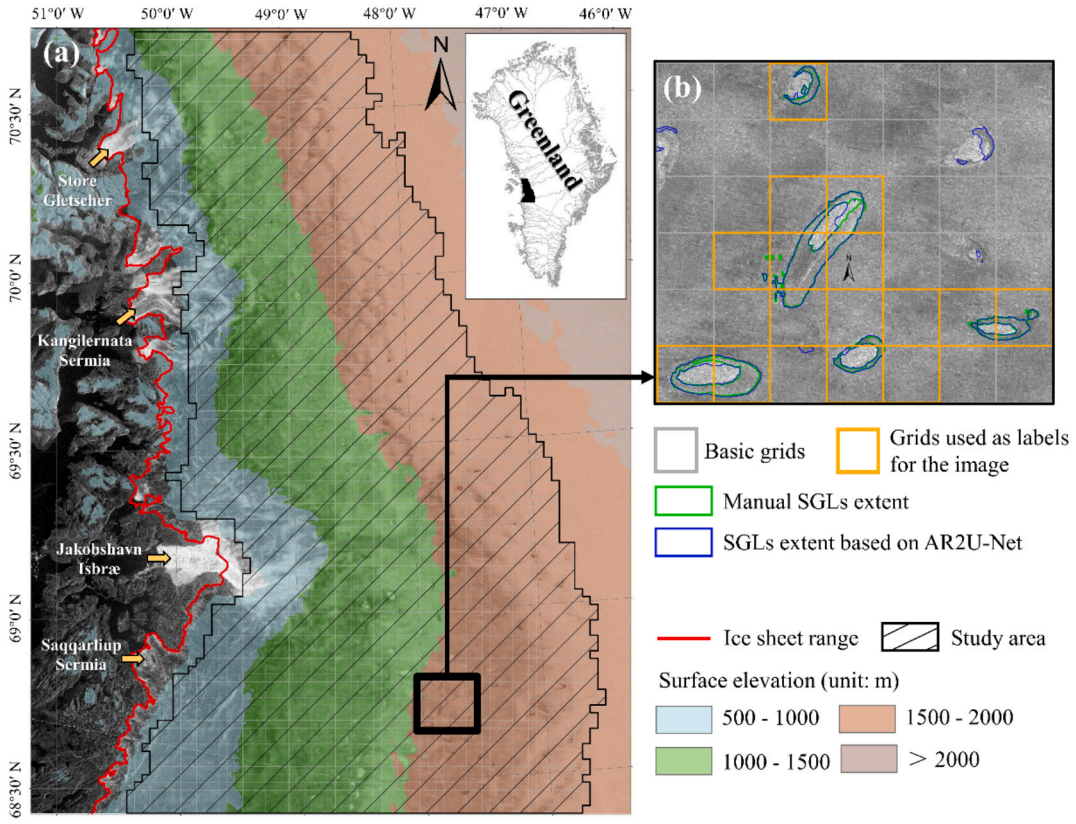

Fig. 1. Location of the study area (a). The background image is a Sentinel-1 HV-polarized image on Feb. 9, 2020. The 256*256 pixels' grid is the base unit for the composition of this study area (grey grids in b). The areas with significant water features are used to produce deep learning labels (orange grids in b). (For interpretation of the references to colour in this figure legend, the reader is referred to the web version of this article.)

Table 1
Date of S1 and S2 images in the experiment. Sixteen time points from 2020 to 2022 containing melt and non-melt seasons.

	Sentinel-1				Sentinel-2
2020	9 Feb	15 May	13 Aug	11 Nov	1 May to 1 Oct
2021	9 Feb	16 May	8 Aug	12 Nov	
2022	10 Feb	17 May	9 Aug	13 Nov	

The SAR images show different characteristics in the SGL and its surrounding snow environment (Fig. 2). In winter, dry snow is almost transparent for the C band, and the main scattering source is the snow–ground interface (Buchelt et al., 2021) and the volume scattering from snowpack (Fig. 2(5)). The dielectric properties of the snowpack considerably change as the snowpack begins to melt. The presence of liquid water in the snowpack decreases the dielectric constant, resulting in a higher absorption coefficient and lower backscattering in the C-band. This phenomenon makes it difficult to distinguish SGLs from snow with high liquid water content (Buchelt et al., 2021). (Fig. 2(3)). When liquid lake forms, the backscatter coefficient of the lake observed in SAR is significantly lower than the surrounding snow (Fig. 2(1) and (4)). After fast drainage of lakes, the slush exhibits an extremely high backscatter coefficient in the SAR image due to the higher surface roughness (Fig. 2(2)).

In the SGLs extraction task using SAR imagery during the non-melt season, HV-polarized SAR imagery is used as the base map, since it better represents water contour information in dry snow imagery.

Based on the locations of SGLs observed during the melt season and the easily accessible SGL contours from HV-polarized SAR imagery during the non-melt season, we performed manual visual interpretation of the SGLs labels in SAR images using ArcMap. Eight SAR images from 2020 and 2021 were used as training and validation data sets for building deep learning models. We augmented the training patches with 1516 pairs labels by clockwise 90°, 180°, and 270° flips, horizontal flips, and vertical flips to expand the training data volume. The final dataset obtained for model building and validation consisted of 9096 pairs. The predicted lake distribution results derived from SAR data from 2020 to 2022 served as the basis for analyzing the annual seasonal variation in SGLs using the established model.

3.3. Deep learning model training

Deep learning methods have been widely applied to the extraction of SGLs from SAR imagery. Several studies have demonstrated that CNN and U-Net models can be effectively applied to SGL extraction (Dirscherl et al., 2021b; Yuan et al., 2020). Therefore, we take the U-Net model as the foundation and introduces two models, namely, AU-Net (Jiang et al., 2022) and AR2U-Net (Zuo et al., 2021), to improve the accuracy of SGL extraction from SAR imagery.

U-net, a popular deep learning foundation network, has spawned various extended models, including AU-Net, residual U-Net (RU-Net), recurrent-residual U-Net (R2U-Net), U-Net++, squeeze+ excite (SE) U-Net, etc. (Kugelman et al., 2022). This study used three models, namely, U-Net, AU-Net, and AR2U-Net, to identify the most suitable model for SGL extraction in the SAR images. U-Net, AU-Net, and AR2U-Net have a similar model framework (Fig. 3). AU-Net integrates U-Net with attention gates, which intensively focus on water body regions. Meanwhile, AR2U-Net integrates AU-Net with recurrent residual convolutional neural network (RRCNN), which further refines feature extraction by iteratively improving segmentation accuracy, especially for blurred water body boundaries in SAR imagery. The semantic segmentation architecture of U-Net includes contracting and expansive paths for up-

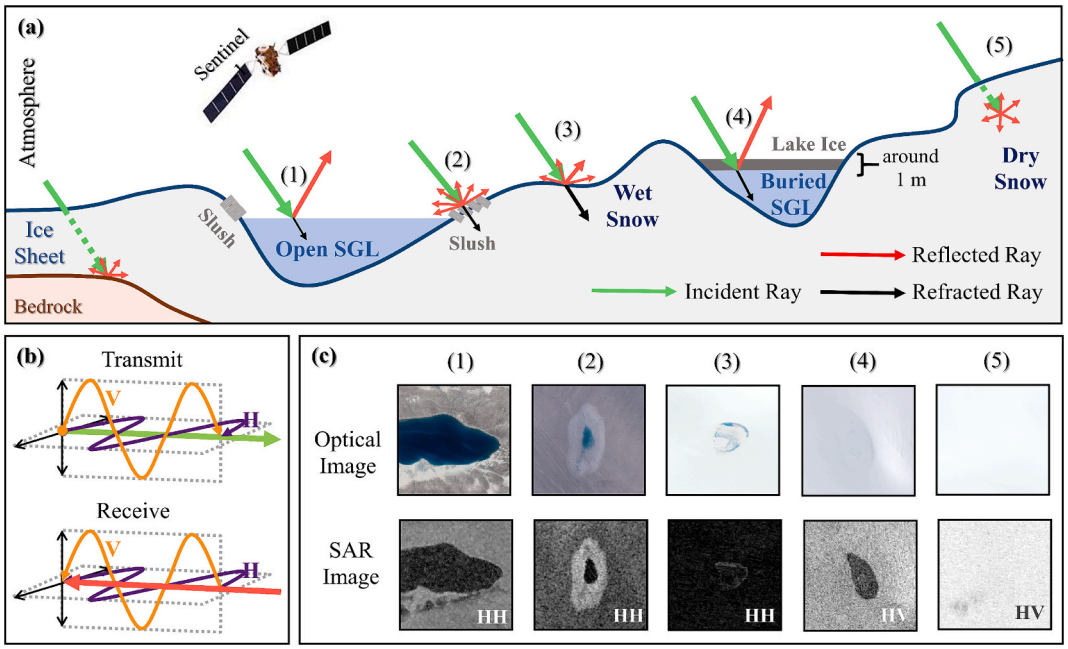

Fig. 2. Schematic illustration of SGL monitoring in Sentinel-1. Open water, buried lake, dry snow, wet snow, and slush exhibit different reflective and refractive rays due to their physical properties (a and b). Consequently, the lake and surrounding snow show differences in the backscatter intensity in the SAR images. HV-polarized is more sensitive than HH-polarized to liquid water content in snow (c (3) and (4)).

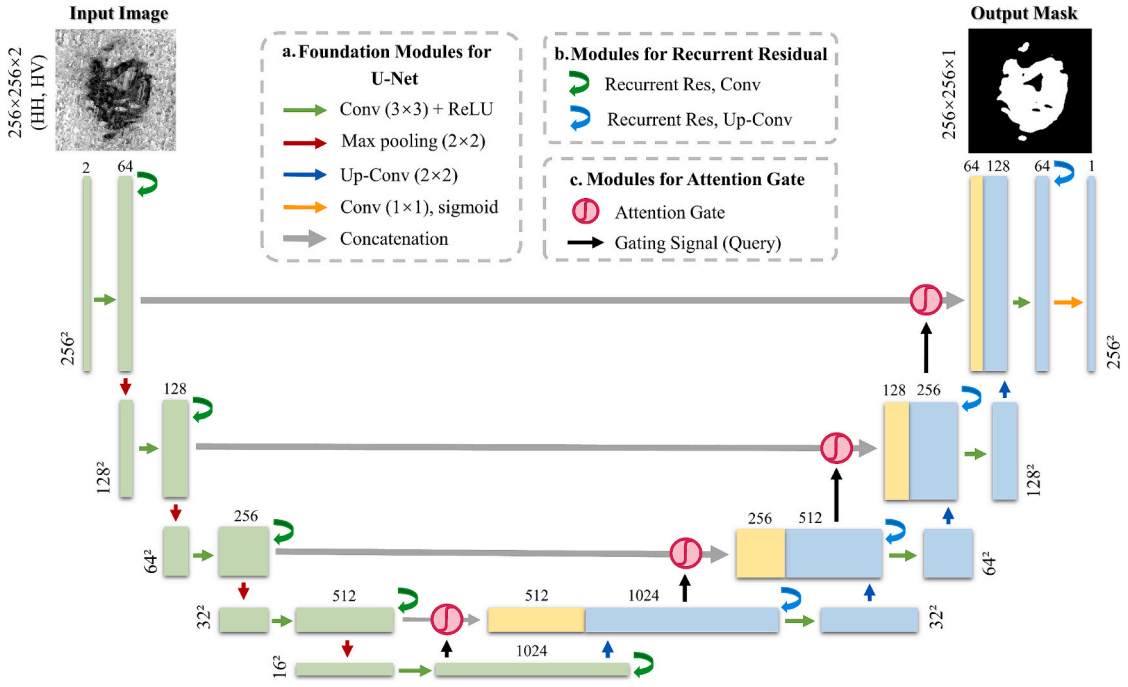

Fig. 3. Diagrams of AR2 U-Net (including parts a, b, and c), U-Net (including part a), and AU-Net (including parts a and c). The input image is HH-polarized SAR image, and the output mask is the predicted result AR2 U-Net.

sampling and down-sampling, utilizing CNN for end-to-end training (Azad et al., 2022). The attention gate guides focus on important regions, while RRCNN aids deep accumulation and feature representation in segmentation tasks (Shim et al., 2022).

The three U-Net based networks were trained on a desktop equipped with an Intel i7-9700 CPU, 32 GB of RAM, and an NVIDIA TITAN RTX with 24 GB of dedicated RAM for 50 epochs. The training settings included a batch size of 8, an Adam optimizer, a learning rate of 0.00001, and a compounding loss function. A dropout layer with a factor of 0.2 was added after the final feature layer to prevent overfitting.

With regard to the loss function, binary cross-entropy (BCE) loss and focal loss were utilized to approximate the value between the target and the expected output. The BCE loss, a cross-entropy loss function for binary classification, is defined as a measure of the difference between two probability distributions.

$$BCELoss = \begin{cases} -\log(p(y_i)), y_i = 1 \\ -\log(1 - p(y_i)), y_i = 0 \end{cases} \quad (1)$$

where y_i represents the true value, which has a value of zero or one; and $p(y_i)$ denotes the predicted value. However, sole reliance on BCE can result in bias toward the background, as water samples were proportionally smaller than the non-water samples (Jaffari et al., 2021), which will make the SGL extraction ineffective. Accordingly, the focal loss function (Azhar & Khodra, 2017) was incorporated, specifically, the binary focal loss. This function focuses on the imbalance between positive and negative samples, enhancing the focus on the harder distinguish samples. Here, we used the focal loss function for binary classification, named binary focal loss, calculated in accordance with Wang et al., (2020):

$$FocalLoss = -\alpha_t(1-p(y_i))^{\gamma}\log(p(y_i)) \tag{2}$$

$$BinaryFocalLoss = \begin{cases} -\alpha(1-p(y_i))^{\gamma}\log(p(y_i)), y_i = 1 \\ -(1-\alpha)p(y_i)^{\gamma}\log(1-p(y_i)), y_i = 0 \end{cases} \tag{3}$$

where α_t term is added to handle the class imbalance problem. α_t is a weighted term whose value is α for positive (foreground) class and $1-\alpha$ for negative (background) class. These labels have fewer water samples than background samples (at around 1: 4). $\alpha = 0.2$ was set to enhance the focus on water after comparison trials. γ is the focus parameter to provide more importance to the hard examples, herein, we set $\gamma = 2$ in the model. The loss function used in the experiments is the mean value of BCE loss and binary focal loss.

After the SGL extent map was extracted by SAR with deep learning models, we post-processed the results for classification, including clump (the convolution kernel is 5) and sieve. Meanwhile, areas with slopes exceeding 15° were removed from the final results to minimize the misclassification of SAR images caused by the radar look angle and terrain relief (Hu et al., 2022).

3.4. Accuracy assessment

The experiments assessed the deep learning model accuracy using the predicted SGL results and corresponding labeled data. The confusion matrix was evaluated using statistical accuracy indicators, including precision (P), recall (R), overall accuracy (OA), F1 score (F1) and mean intersection over union (MIoU). The confusion matrix shows the relationship between the actual and the predicted classes, and it contains the number of true positive pixels (TP), true negatives pixels (TN), false positive pixels (FP), and false negatives pixels (FN). The statistical accuracy indicators are calculated from TP, TN, FP, and FN.

$$\mathrm{P} = \frac{TP}{TP+FP} \tag{4}$$

$$\mathrm{R} = \frac{TP}{TP+FN} \tag{5}$$

$$\mathrm{OA} = \frac{TP+TN}{TP+TN+FP+FN} \tag{6}$$

In the case of unbalanced samples, a single P, OA, and R cannot efficiently measure the quality of the results. A trade-off occurs between P and R, specifically, improving P typically reduces R, and vice versa. Accordingly, we calculated the F1 to find an equal balance between P and R, which is useful in evaluating imbalanced binary classification. Meanwhile, MIoU provides a robust evaluation by quantifying the overlap between the predicted results and the ground truth, which is a critical metric in segmentation tasks (Kaushik et al., 2025).

$$\mathrm{F1} = 2^{*}\frac{\mathrm{Precision}\times\mathrm{Recall}}{\mathrm{Precision}+\mathrm{Recall}} \tag{7}$$

$$\mathrm{MIoU} = \frac{1}{\mathrm{k}}\sum_{i=1}^{k}\frac{\mathrm{TP}}{\mathrm{TP}+\mathrm{FP}+\mathrm{FN}} \tag{8}$$

4. Results and discussion

4.1. Models' classification results

The experiment involved comparison of three randomly divided datasets (training, validation, and test sets in a 6:2:2 ratio) using U-Net, AU-Net, and AR2U-Net models. We designed three random sample splits, which were applied across multiple deep learning models. Averaging the results from multiple experiments effectively helps in reducing the potential for falsely high accuracy due to labels with spatial autocorrelation. The average validation accuracies are demonstrated in Table 2. AR2U-Net outperforms U-Net and AU-Net, with higher P, R, F1, MioU, and OA (96.1% in OA). However, AR2U-Net's greater network depth results in three times model parameters and double the computing time.

The average of the absolute deviations across the three sets are all below 0.03, indicating that the three models have high stability under different random divisions. The AU-Net and AR2U-Ne with attention gates have minimal fluctuation in the average of the F1, MIoU and OA, with the average of the absolute deviations less than 0.006. This result demonstrates the promising performance of the model with the attention gate module in SGL extraction from the SAR images.

Fig. 4 shows the extraction results of the nine typical SGLs under three deep learning models, with AR2U-Net producing results closer to the ground truth. Fig. 4a exhibits an open water lake/lake with a thin ice cover, which forms during the melting season and can be efficiently extracted by all deep learning models in our experiment. In terms of SGL extraction details, although AR2U-Net is moderately optimized compared with the U-Net and AU-Net (Fig. 4b–e), errors persist, such as poor extraction of meltwater in ice crevasses (Fig. 4c) and finer linear water (Fig. 4d). This situation is primarily due to severe speckle noise interference in SAR images displaying linear features (Zhou et al., 2011). Subjective errors in label production also affect the extraction of lake detail. Overall, the results obtained by AR2U-Net are highly consistent with the general SGL pattern in SAR images relative to the ground truth in the connected lake portion (Fig. 4f–g). In Fig. 4h–i, AR2U-Net is the most effective in minimizing the effects of slope shadows and wet snow among all models.

After the comparison of the three deep learning models, we utilized the AR2U-Net model for SGL extraction. AR2U-Net integrates R2U-Net convolution neural networks with attention gates, where the R2U-Net can increase performance with the same input to enhance segmentation performance, and the attention mechanism can suppress irrelevant background features (Shim et al., 2022). AR2U-Net deepens the network while minimizing gradient errors, and it can improve network features or model performance under the same parameters. In this study, deep learning facilitates effective SGL extraction in water areas. Nonetheless, SAR labelling is labor-intensive and subjective. Although this study selected the labelling areas with the assistance of optical images, the amount of labelling still needs to be further expanded.

4.2. Accuracy assessment

We evaluated the extraction accuracy of SGLs in different seasons (February, May, August, and November) based on AR2U-Net. Fig. 5a

Table 2
Parameters of the accuracy assessment for U-Net, AU-Net and AR2U-Net based on three sets of randomly partitioned datasets (the arithmetic mean of three random splits).

	Params (MB)	P	Recall	OA	F1	MIoU
U-Net	119.7	0.807	0.782	0.936	0.794	0.793
AU-Net	121.7	0.829	0.851	0.949	0.840	0.832
AR2U-Net	368.2	**0.850**	**0.905**	**0.961**	**0.877**	**0.867**

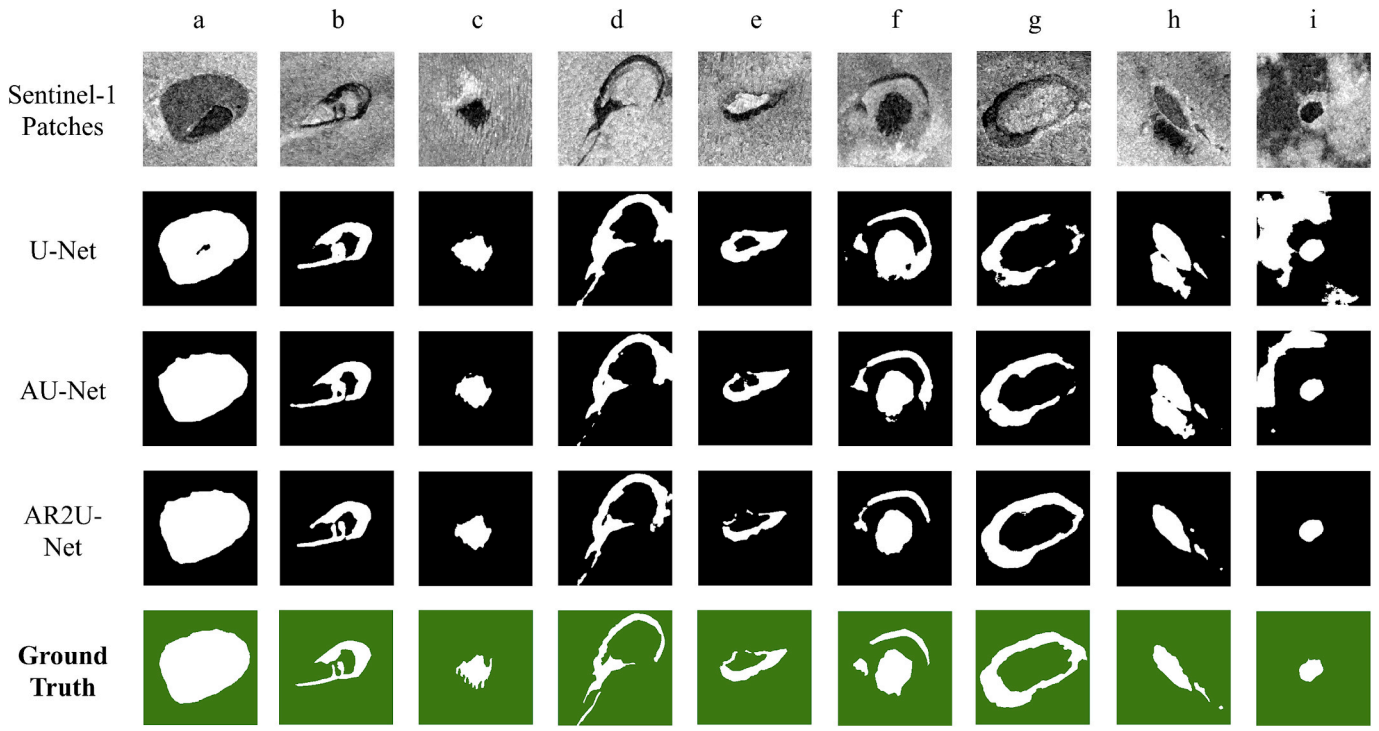

Fig. 4. Comparison of the U-Net, AU-Net, and AR2U-Net results for typical SGLs.

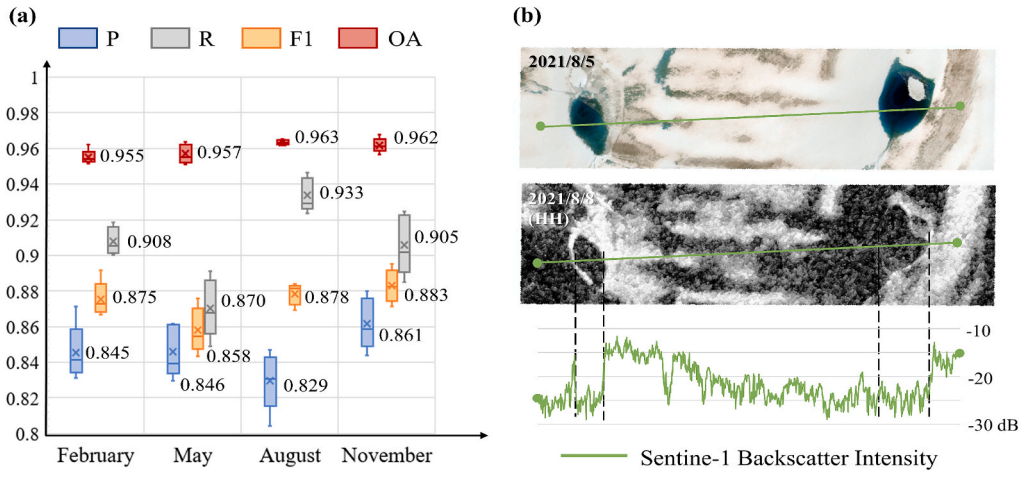

Fig. 5. Evaluation of the extraction accuracy for the different months based on AR2U-Net (a). Part of the SGLs are difficult to accurately extract because their SAR image features are close to the surroundings (b).

demonstrates the multi-month accuracy results of AR2U-Net that trained five randomly divided datasets. OA and F1 are a combined evaluation of non-water and water classification results. Meanwhile, P and R are individual evaluations of the effectiveness of water extraction. The AR2U-Net classification results show a high OA in all seasons ranging from 0.955 to 0.963 and F1 from 0.858 to 0.883. These results minimally varied across months, indicating that the month differences in the input labels did not have a significant effect on the overall prediction. P and R significantly varied across the months (Fig. 5a), with R consistently higher than P. The calculation expressions of R and P demonstrated that the differences are mainly in the form of larger FP and smaller FN, that is, non-water areas are misidentified as SGLs in some cases.

The value discrepancy caused by misclassification, reflected in R and P, is particularly evident in the August results. This is presumably due to high snow moisture on the ice sheet's surface during Greenland's melt season. Deep learning approaches have shown good results in removing slope shadows and wet snow effects for SGL extraction (Fig. 4h–i). However, these effects cannot be completely resolved, and some affected lakes remain challenging to separate (Fig. 5b). Wet snow has strong absorption, causing a sharp decline in the intensity of the backscattering echo in SAR images (Liang et al., 2021), making it difficult to distinguish between wet snow and lakes. The optical and SAR images of the two typical SGLs in the melting zone are shown in Fig. 5b. The extent of the SGLs is clearly in the optical image but hard to distinguish in the HH-polarized SAR image. The backscatter intensity of the wet snow and the SGLs is around −25 dB, making it impossible to extract the lake by the threshold. The SGL on the left is easier to identify due to its separate lake morphology, while the lake on the right is more difficult to extract due to its high similarity to surroundings. This extraction error, concentrated mainly in the melting period, is a significant source of SGL

misclassification using SAR images.

The multiple accuracy indicators for each month show that the extraction of SGLs from SAR images in the non-melt season is better than that in the melt season, with the highest accuracy in November. In summary, SAR images in the melt season are poor for extracting SGLs due to the influence of snow moisture and highly suitable in the non-melt season. Nevertheless, buried lakes still exist at high altitudes during the melt season, and showing the entire picture of SGLs during the melt season using optical imagery alone present challenges. Future research should discuss the overall surface/subsurface meltwater distribution at different altitudes during the melt season by combining multi-source remote sensing.

4.3. Distribution of SGLs

The study predicted SGL distribution in the study area for February, May, August, and November from 2020 to 2022 using $NDWI_{ice}$ and the AR2U-Net model. Considering that SAR images are significantly affected by surface melting during summer, resulting in poor SGL extraction, optically extracted results were incorporated to aid the discussion on SGL distribution during the melt season (Fig. 6). The green, red, and blue regions represented SGL areas extracted from SAR images at nine non-melting time points over three years, while the orange region represented the maximal lake range during the melt season. The maximum water range, derived from the SGL mask extracted from S2 images from 1 May to 1 October each year, represented the maximum SGL area during the melting season (Zheng et al., 2023; Zhu et al., 2023).

In February and May across the 3 year period, the monitored SGL area in the study area was relatively small (around 200 km^2). In November, post-melt season, the SGL area based on the SAR images was much larger than that in February and May (before the melt season), measuring 343.42, 263.40, and 412.02 km^2 from 2020 to 2022. The presence of water in November suggested that some lakes remained subsurface after the melt season, existing as buried lakes. Some lakes persisted through the next year's melt season, while others were drained and refrozen during the non-melt season (Koenig et al., 2015; Lampkin

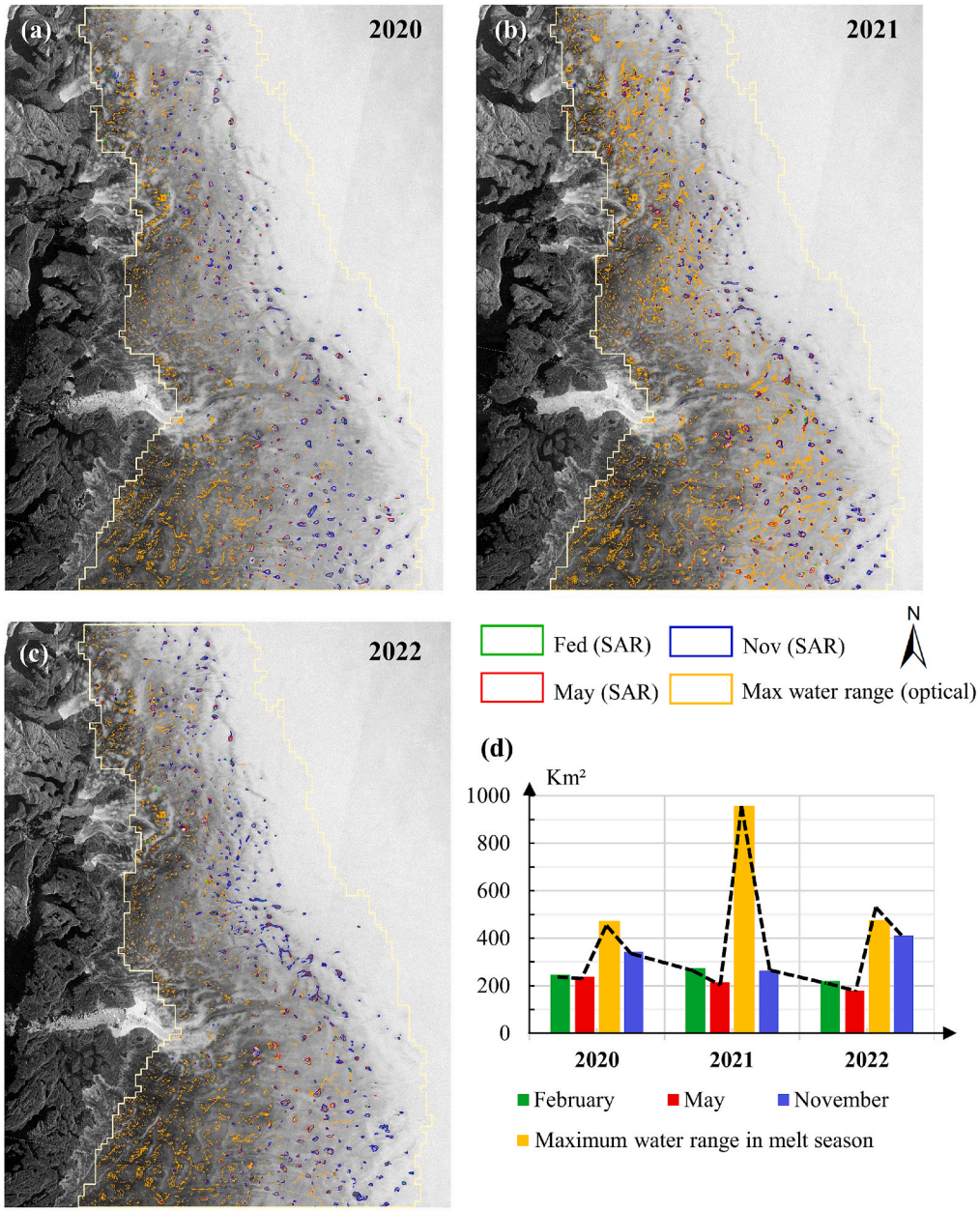

Fig. 6. Schematic illustration of the changes in the distribution (a–c) and area (d) of the SGLs in the study area from 2020 to 2022.

et al., 2020; Zhou et al., 2011). The water area detected during the non-melt season exhibited a continuous decreasing trend based on the temporal changes in the lake area during one non-melt season. The largest water area was monitored in November 2022 during the 3 year non-melt season, possibly due to an unusual amount of melt and meltwater runoff in September 2022 caused by a late-season heatwave over southeasternmost Greenland, extending the melt season in 2022 (NSIDC's Greenland Today blog).

The maximum water range was used as the SGL extent in the melt season to explore the relationship between lake changes in the non-melt and melt seasons. In the maximum water range obtained from S2 images for the 3 year melt season, 2021 has the largest SGL area of 953.85 km^2, nearly twice as large as the SGL area in the 2020 and 2022 melt seasons. The large lake area in 2021 was mainly reflected in the presence of numerous reticulated water systems, frequently occurring at elevations above 1500 m (Fig. 6a–c). The climate data showed that an atmospheric river delivered extreme rainfall events at the GrIS summit in 2021, resulting in intense ice sheet snowmelt, which may have enhanced snowmelt at high elevations (Box et al., 2022). In 2020, few reticulation water systems were detected. By 2022, some reticulated water systems were present at elevations around 1800 m. The region of the reticulated water system is concentrated on the southern side of Jakobshavn Isbræ in the study area, which was detected to have a rich river system (Smith et al., 2015; Yang et al., 2021). The decrease in SGL area at the end of the melt season, illustrated by the line graph in Fig. 6d, is not dramatic in 2020 and 2022. This result is inconsistent with Zheng et al.'s (2023) discussion that only about 13% of the summer SGLs in Greenland can persist through winter. A discrepancy exists because the area of SGLs acquired in this experiment based on SAR images includes buried lakes that frequently occur at high elevations and do not open throughout the year (Miles et al., 2017). These lakes cannot be detected in the optical images; therefore, they are not within the scope of Zheng's study discussion.

4.4. Comparison between melting and non-melting seasons

Overlapping and independence area exist in the visible ranges of the SGLs on the optical and SAR images. The SAR image can access buried lakes, which may remain after the melt season or never open throughout the year, under a shallow snow cover. The optical image can detect the open water during the melt season and monitor the lifecycle of the SGL that is fully drained in the melt season. However, the association of changes in the SGLs between the melt and the non-melt seasons is complex, including refreezing, complete drainage, and incomplete drainage. We compared the maximum water range extracted with Sentinel-2 and the lakes extracted with Sentinel-1 (May and November) of each year (Fig. 7, Table 3) in this section. The objective was to analyze the seasonal changes in the presence, spatial extent, and retention or drainage status of liquid water in SGLs between the melt and non-melt seasons.

We represented the area changes in SGLs in the form of grid types to interpret their spatial distribution across different time points. These grids are categorized into eight types depending on the time points of SGL existence in each grid. Types 1–4 exhibit the sources and destinations of SGLs during the melt season. Meanwhile, types 5–7 exhibit the areas of buried lakes that cannot be detected in optical imagery. The lake detected during the melting season may form in the current melting season (types 3 and 4) or originate from buried lakes that already existed before the melting season (types 1 and 2). Some buried lakes may have complete drainage before the coming melt season (type 5). At the end of current melt season, parts of the SGLs were completely discharged (types 2 and 3). Meanwhile, some SGLs were retained to form buried lakes (types 1 and 4). Furthermore, the experiments detected buried lakes that

Table 3
Area of SGLs in the study area at different time intervals from 2020 to 2022.

Type	Months of lake existence			Area in each year (km^2)		
	May.	Aug.	Nov.	2020	2021	2022
1	√	√	√	23.624	40.841	16.753
2	√	√		22.117	56.183	14.505
3		√		332.487	778.805	357.058
4		√	√	90.366	78.003	84.298
5	√			68.106	65.763	45.139
6			√	104.552	92.580	207.437
7	√		√	124.876	51.973	103.531

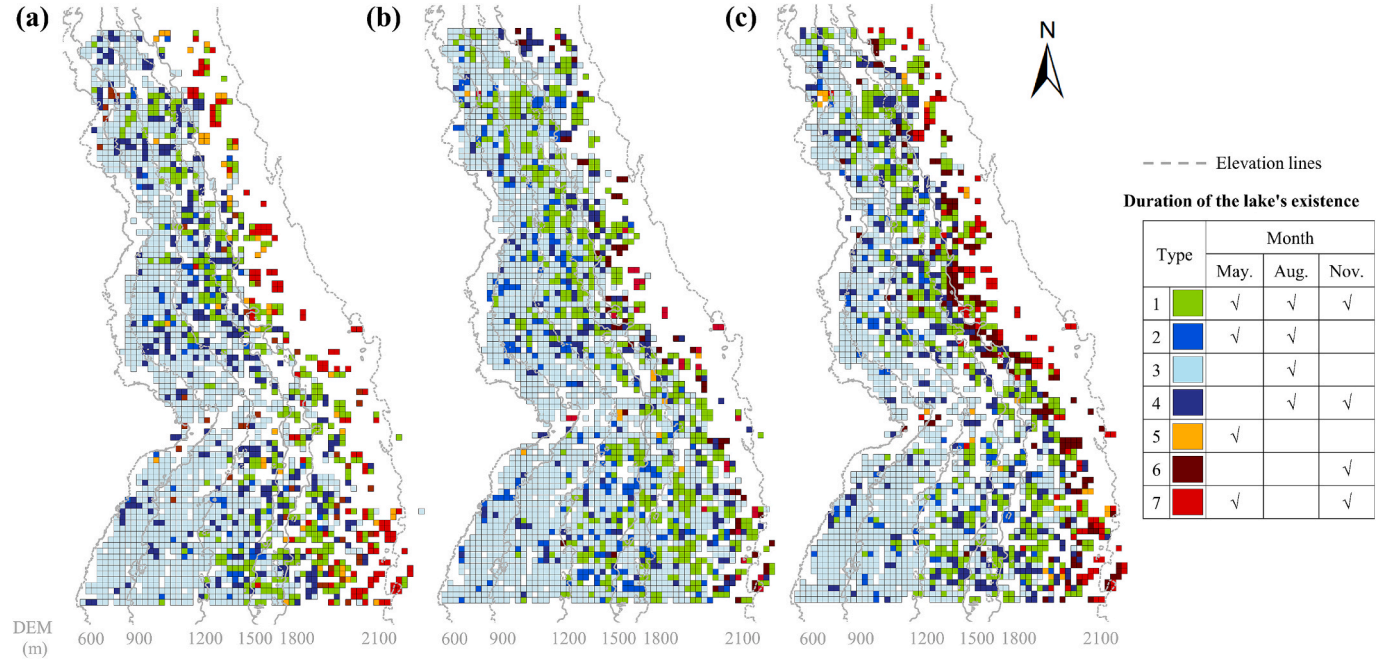

Fig. 7. Distributions of SGL existence in the study area at different time points, including the water storage during the melt season (August) and before and after the melt season (May and November) from 2020 to 2022 (a–c).

separately existed before and after the melt season (types 5, 6, and 7), which were not detected in the melt season imagery. The absence of water in those lakes during the melting season cannot be asserted, as the water in those regions may not be visible in optical imagery, resulting a gap in the melting season data. This phenomenon highlights limitation of solely relying on optical imagery to assess the SGL distribution during the melting season, as buried lakes in high-altitude regions are challenging to detect.

The number of grids detected for the SGLs in the 3 years are 2176, 2680, and 2228, with the water range being the most widely monitored in 2021. The grid numbers detected by optical images in the 3 years are 1966, 2578, and 1947, with a wide range of detection in 2021. The grid numbers detected by SAR images are 931, 1022, and 1103, with a slightly wider range of detection in 2022. In terms of elevation distribution, the buried lakes are widely distributed before the melt season (types 1, 2, and 5). Water stored at lower elevations is susceptible to drainage in the middle of the melt season (type 2). Meanwhile, water stored at medium to high elevations (>1200 m) is more likely to be retained until the end of the melt season (type 1). In the newly formed SGLs during the melt season (type 3 and 4), lakes in higher elevations are more likely to be preserved at the end of the melt season, typically higher than 1200 m. In the region around 2000 m elevation, SGLs are difficult to detect during the melt season. Nonetheless, a number of buried lakes can be detected in the SAR images (types 6 and 7).

The area changes of the different types in 2020, 2021, and 2022 show that:

(1) The areas of buried lakes that existed in the late melt season but are not detected in the melt season (types 6 and 7) in 3 years were 229.428, 144.543, and 310.969 km^2. The smallest area of those lakes was found in 2021, mainly because the melt was the most extensive in 2021 (Box et al., 2022), with most of the buried lakes areas opened during the melt season (Table 3), resulting in a smaller lake area detected only in the SAR imagery.
(2) More buried lakes were observed after the melting season in 2022 (Fig. 7, Table 3). This phenomenon may be associated with the later peak melt in September 2022. The peak melting in Greenland typically occurs in July and August, and the surface melting of the ice sheet gradually decreases after September. However, in 2022, the extreme air pressure and hurricanes affecting the Greenland resulting in a significant melting peak in September. After the extreme heat in September, temperatures sharply dropped, possibly causing a rapid refreezing of melting snow and forming a shallow, widespread, and impermeable layer on ice sheet surface (MacFerrin et al., 2019). These impermeable areas may have hindered the drainage of SGLs, resulting in the formation of more buried lakes after the 2022 melting season.
(3) The area of buried lakes not monitored in the optical imagery (types 6 and 7) are much larger compared with the buried lakes (types 1 and 4), which are stored by open water during the melt season. The area summation of latter types is twice as large as the area summation of the former types in 2020, three times as large in 2022, and only flat in 2021, when melting is most intense. This notion suggests that the ice sheet has a great deal of water storage in the form of buried lakes, and those lakes are present in the ice sheet all year round (Koenig et al., 2015; Law et al., 2020).
(4) In this study, majority of meltwater in the melt season originated from surface melting during the new summer, with only 5%–10% originating from buried lakes left over from the previous melt season. Approximately 78%–91% of the meltwater generated in new summer is completely drained during the melt season, and only 9%–22%, with a mean value of 16.52%, is retained to form a buried lake. This discovery aligns with the observation that about 13% of the summer SGLs in Greenland can persist through winter (Zheng et al., 2023). The storage capacity of the buried lake is vast, and only a small part of it comes from the meltwater produced during the new melt season. In the SGLs produced during the new melt season of 3 years, water lost during the 2020 and 2022 melt seasons was around 80%, and water drained during the 2021 melt season reached 90%, with a small difference in the final remaining buried lake area (type 4) in 3 years. Substantial extensive summer melt will result in significant amounts of surface runoff. However, the area changes of buried lake are insensitive to the intensity of ice sheet melting, as the difference in residual water area between high and normal melt years was below 20 km^2.

5. Conclusions

SGLs are a significance component of the ice sheet hydrological network, closely related to the ice sheet mass balance and sea level change. In recent years, variations in SGLs due to rising global temperatures and frequent extreme climatic phenomena have attracted the wide attention of scholars. Although experiments have shown that SGLs exist throughout the year, and the water is stored in buried lakes during the non-melt season, studies that focused on the SGL changes at year-round scales are still scarce. Moreover, no SGL study that incorporated multi-source remote sensing satellite data have extensively discussed the water storage changes of the different SGL types.

In this study, we extracted SGLs from the optical and SAR images using deep learning methods in southwest GrIS at 12 time points of 2020 to 2022. The experiment performed the S1-based label production and whole study area SGL prediction in February, May, August, and November from study period. Three deep learning models, namely, U-Net, AU-Net, and AR2U-Net, were used for comparison. The AR2U-Net model showed the best results for SGL extraction with the highest average precision parameters and contained more lake details. Nevertheless, the model results during the melt season were unsatisfactory, primarily because the wet snow has approximate backscattering intensity to SGLs in the SAR images. This situation made it difficult to distinguish lakes from the higher snow moisture region from their surroundings. Considerable details of the buried lake can be detected in the SAR imagery during the non-melt season compared with the SAR extraction results, which were unsatisfactory during the melt season.

Differences in the monitored SGLs for the corresponding months of each year from 2020 to 2022 were insignificant, with the main divergence stemming from some extreme climate phenomena, such as the extreme atmospheric river in 2021 and the later peak melt in 2022. Buried lakes exist throughout the year in the study area, and they have slowly decreased in area from November during the non-melt season to February and May of the following year. In terms of the spatial and temporal changes of the SGLs in the study area from 2020 to 2022, the SGLs at lower elevations are more active during the melt season with complete storage-drainage events. Meanwhile, the SGLs at medium to high elevations (>1200 m) are more likely to be stored as buried lakes at the end of the melt season. During 3-year melt seasons, 78%–91% of the newly generated meltwater was drained, and only about 16.52% formed as buried lakes. The area of buried lakes left the from new melt season was insensitive to the intensity of melting, which may relate to the generation of surface runoff during the melt season. Furthermore, the extent of buried lakes formed from the new melt season is only one-third to one-half of the area of the year-round closed buried lakes monitored by the SAR, demonstrating a significant amount of subsurface water storage on the surface of the ice sheet, which is often overlooked in the analyses of year-round changes of SGLs.

The SGL change should be discussed by using multi-source remote sensing data, which links the open lakes during the melt season and the buried lakes during the non-melt season to explore the changes in water storage on the ice sheet surface. Meanwhile, deep learning methods show advantages in SGL extraction in complex situations, although the workload is higher in pre-preparation and the subjectivity of label creation is inevitable. In the future, this study should expand the dataset

and extend the SGL prediction to the entire Greenland Ice Sheet and potentially the Antarctic Ice Sheet, to provide comprehensive data support for exploring the hydrological information of the ice sheet surface. More methods for extracting SGLs need to be explored, including how to combine SAR and optical imagery during the melt season to obtain a more comprehensive and objective coverage of lakes. Concurrently, data on SGL changes can be combined with the ice sheet phenology information, resulting in further discussion of the response to extreme climate events and their impact on the ice sheet's mass balance.

CRediT authorship contribution statement

Dongyu Zhu: Writing – original draft, Methodology, Formal analysis, Data curation, Conceptualization. **Chunxia Zhou:** Project administration, Funding acquisition, Conceptualization. **Xiaoli Chen:** Writing – review & editing, Formal analysis, Data curation. **Jiani Ouyang:** Validation, Software, Methodology. **Ce Zhang:** Supervision, Project administration.

Declaration of competing interest

The authors declare that they have no known competing financial interests or personal relationships that could have appeared to influence the work reported in this paper.

Acknowledgments

This research is funded by the National Key Research and Development Program of China (2021YFC2803302, 2021YFC2803303), the National Natural Science Foundation of China (NSFC) (42171133), and is also sponsored by the China Scholarship Council (CSC).

Data availability

Data will be made available on request.

References

Azad, R., Aghdam, E.K., Rauland, A., Jia, Y., Avval, A.H., Bozorgpour, A., Karimijafarbigloo, S., Cohen, J.P., Adeli, E., Merhof, D., 2022. *Medical Image Segmentation Review: The success of U-Net*. 1–38.

Azhar, A.N., Khodra, M.L., 2017. Focal loss for dense object detection. In: Proceedings of the IEEE International Conference on Computer Vision (ICCV), pp. 2980–2988. https://doi.org/10.1109/ICAICTA49861.2020.9428882.

Benedek, C., Willis, I., 2020. Winter drainage of surface lakes on the Greenland ice sheet from sentinel-1 SAR imagery. Cryosphere Discuss. May, 1–25. https://doi.org/10.5194/tc-2020-70.

Box, J.E., Wehrlé, A., As, D. Van, Fausto, R.S., Kjeldsen, K.K., Dachauer, A., Ahlstrøm, A. P., Picard, G., 2022. *Greenland Ice Sheet Rainfall, Heat and Albedo Feedback Impacts From the Mid-August 2021 Atmospheric River. August 2021*. https://doi.org/10.1029/2021GL097356.

Buchelt, S., Skov, K., Ullmann, T., 2021. Sentinel-1 time series for mapping snow cover and timing of snowmelt in Arctic periglacial environments: case study from the Zackenberg Valley, Greenland. Cryosphere Discussions 1–24.

Chouksey, A., Thakur, P.K., Sahni, G., Swain, A.K., Aggarwal, S.P., Kumar, A.S., 2021. Mapping and identification of ice-sheet and glacier features using optical and SAR data in parts of central Dronning Maud Land (cDML), East Antarctica. Polar Sci. 30 (August), 100740. https://doi.org/10.1016/j.polar.2021.100740.

Dirscherl, M., Dietz, A.J., Kneisel, C., Kuenzer, C., 2021a. A novel method for automated supraglacial lake mapping in antarctica using sentinel-1 sar imagery and deep learning. Remote Sens. (Basel) 13 (2), 1–27. https://doi.org/10.3390/rs13020197.

Dirscherl, M., Dietz, A.J., Kneisel, C., Kuenzer, C., 2021b. A novel method for automated supraglacial lake mapping in antarctica using sentinel-1 sar imagery and deep learning. Remote Sens. (Basel) 13, 1–27. https://doi.org/10.3390/rs13020197.

Dirscherl, M., Dietz, A., Kuenzer, C., 2022. *Artificial intelligence for the monitoring of Antarctic supraglacial lake dynamics in 2015-2021 using Sentinel-1 SAR and optical Sentinel-2 data*.

Dunmire, D., Banwell, A.F., Wever, N., Lenaerts, J.T.M., Datta, R.T., 2021. Contrasting regional variability of buried meltwater extent over 2 years across the Greenland Ice Sheet. Cryosphere 15, 2983–3005. https://doi.org/10.5194/tc-15-2983-2021.

Felikson, D., Bartholomaus, T.C., Catania, G.A., Korsgaard, N.J., Kjær, K.H., Morlighem, M., Noël, B., Broeke, M.V., Stearns, L.A., Shroyer, E.L., Sutherland, D.A., Nash, J.D., 2017. Inland thinning on the Greenland ice sheet controlled by outlet glacier geometry. Nat. Geosci. 10 (April). https://doi.org/10.1038/NGEO2934.

Hoffman, M.J., Perego, M., Andrews, L.C., Price, S.F., Neumann, T.A., Johnson, J.V., Catania, G., Lüthi, M.P., 2018. Widespread moulin formation during supraglacial lake drainages in Greenland. Geophys. Res. Lett. 45 (2), 778–788. https://doi.org/10.1002/2017GL075659.

Hu, J., Huang, H., Chi, Z., Cheng, X., Wei, Z., Chen, P., Xu, X., Qi, S., Xu, Y., Zheng, Y., 2022. er. *Remote Sensing*, *14*(1). https://doi.org/10.3390/rs14010055.

Jaffari, R., Hashmani, M.A., Reyes-Aldasoro, C.C., 2021. A novel focal phi loss for power line segmentation with auxiliary classifier u-net. Sensors 21 (8). https://doi.org/10.3390/s21082803.

Jiang, D., Li, X., Zhang, K., Marinsek, S., Hong, W., Wu, Y., 2022. Automatic supraglacial lake extraction in Greenland using sentinel-1 SAR images and attention-based U-Net. Remote Sens. (Basel) 14 (19). https://doi.org/10.3390/rs14194998.

Johansson, A.M., Brown, I.A., 2012. Observations of supra-glacial lakes in west Greenland using winter wide swath Synthetic Aperture Radar. Remote Sens. Lett. 3 (6), 531–539. https://doi.org/10.1080/01431161.2011.637527.

Kaushik, S., Maurya, L., Tellman, E., Zhang, G., Dharpure, J.K., 2025. Science of Remote Sensing Debris covered glacier mapping using newly annotated multisource remote sensing data and geo-foundational model. Sci. Remote Sens. 12 (October), 100319. https://doi.org/10.1016/j.srs.2025.100319.

Koenig, L.S., Lampkin, D.J., Montgomery, L.N., Hamilton, S.L., Turrin, J.B., Joseph, C.A., Moutsafa, S.E., Panzer, B., Casey, K.A., Paden, J.D., Leuschen, C., Gogineni, P., 2015. Wintertime storage of water in buried supraglacial lakes across the Greenland Ice Sheet. Cryosphere 9 (4), 1333–1342. https://doi.org/10.5194/tc-9-1333-2015.

Kugelman, J., Allman, J., Read, S.A., Vincent, S.J., Tong, J., Kalloniatis, M., Chen, F.K., Collins, M.J., Alonso-Caneiro, D., 2022. A comparison of deep learning U-Net architectures for posterior segment OCT retinal layer segmentation. Sci. Rep. 12 (1), 1–14. https://doi.org/10.1038/s41598-022-18646-2.

Lampkin, D.J., Koenig, L., Joseph, C., Box, J.E., 2020. Investigating controls on the formation and distribution of wintertime storage of water in supraglacial lakes. Front. Earth Sci. 8 (November), 1–19. https://doi.org/10.3389/feart.2020.00370.

Law, R., Arnold, N., Benedek, C., Tedesco, M., Banwell, A., Willis, I., 2020. Over-winter persistence of supraglacial lakes on the Greenland Ice Sheet: results and insights from a new model. J. Glaciol. 66 (257), 362–372. https://doi.org/10.1017/jog.2020.7.

Leeson, A.A., 2020. Evolution of Supraglacial Lakes on the Larsen B Ice Shelf in the Decades Before it Collapsed Geophysical Research Letters. Figure 1, 1–9. https://doi.org/10.1029/2019GL085591.

Liang, D., Guo, H., Zhang, L., Cheng, Y., Zhu, Q., Liu, X., 2021. Time-series snowmelt detection over the Antarctic using Sentinel-1 SAR images on Google Earth Engine. Remote Sens. Environ. 256, 112318. https://doi.org/10.1016/j.rse.2021.112318.

MacFerrin, M., Machguth, H., van As, D., Charalampidis, C., Stevens, C.M., Heilig, A., Vandecrux, B., Langen, P.L., Mottram, R., Fettweis, X., Broeke, M.R., Pfeffer, W.T., Moussavi, M.S., Abdalati, W., 2019. Rapid expansion of Greenland's low-permeability ice slabs. Nature 573 (7774), 403–407. https://doi.org/10.1038/s41586-019-1550-3.

Miles, K.E., Willis, I.C., Benedek, C.L., Williamson, A.G., Tedesco, M., 2017. Toward monitoring surface and subsurface lakes on the Greenland ice sheet using sentinel-1 SAR and landsat-8 OLI imagery. Front. Earth Sci. 5 (July), 1–17. https://doi.org/10.3389/feart.2017.00058.

Morlighem, M., Williams, C.N., Rignot, E., An, L., Arndt, J.E., Bamber, J.L., Catania, G., Chauché, N., Dowdeswell, J.A., Dorschel, B., Fenty, I., Hogan, K., Howat, I., Hubbard, A., Jakobsson, M., Jordan, T.M., Kjeldsen, K.K., Millan, R., Mayer, L., Zinglersen, K.B., 2017. BedMachine v3: complete bed topography and ocean bathymetry mapping of greenland from multibeam echo sounding combined with mass conservation. Geophys. Res. Lett. 44 (21), 11051–11061. https://doi.org/10.1002/2017GL074954.

Moussavi, M., Pope, A., Halberstadt, A.R.W., Trusel, L.D., Cioffi, L., Abdalat, W., 2020. Antarctic supraglacial lake detection using landsat 8 and sentinel-2 imagery: towards continental generation of lake volumes. Remote Sens. (Basel) 12 (1). https://doi.org/10.3390/RS12010134.

Mullissa, A., Vollrath, A., Odongo-Braun, C., Slagter, B., Balling, J., Gou, Y., Gorelick, N., Reiche, J., 2021. Sentinel-1 sar backscatter analysis ready data preparation in google earth engine. Remote Sens. (Basel) 13 (10), 5–11. https://doi.org/10.3390/rs13101954.

Shim, J.H., Kim, W.S., Kim, K.G., Yee, G.T., Kim, Y.J., Jeong, T.S., 2022. Evaluation of U-Net models in automated cervical spine and cranial bone segmentation using X-ray images for traumatic atlanto-occipital dislocation diagnosis. Sci. Rep. 12 (1), 1–10. https://doi.org/10.1038/s41598-022-23863-w.

Smith, L.C., Chu, V.W., Yang, K., Gleason, C.J., Pitcher, L.H., Rennermalm, A.K., Legleiter, C.J., Behar, A.E., Overstreet, B.T., Moustafa, S.E., Tedesco, M., Forster, R. R., LeWinter, A.L., Finnegan, D.C., Sheng, Y., Balog, J., 2015. Efficient meltwater drainage through supraglacial streams and rivers on the southwest Greenland ice sheet. PNAS 112 (4), 1001–1006. https://doi.org/10.1073/pnas.1413024112.

Smith, L.C., Yang, K., Pitcher, L.H., Overstreet, B.T., Chu, V.W., Rennermalm, Å.K., Ryan, J.C., Cooper, M.G., Gleason, C.J., Tedesco, M., Jeyaratnam, J., Van As, D., Van Den Broeke, M.R., Van De Berg, W.J., Noël, B., Langen, P.L., Cullather, R.I., Zhao, B., Willis, M.J., Behar, A.E., 2017. Direct measurements of meltwater runoff on the Greenland ice sheet surface. PNAS 114 (50), E10622–E10631. https://doi.org/10.1073/pnas.1707743114.

Spergel, J.J., Kingslake, J., Creyts, T., Van Wessem, M., Fricker, H.A., 2021. Surface meltwater drainage and ponding on Amery Ice Shelf, East Antarctica, 1973-2019. J. Glaciol. https://doi.org/10.1017/jog.2021.46.

Trusel, L.D., Das, S.B., Osman, M.B., Evans, M.J., Smith, B.E., Fettweis, X., McConnell, J. R., Noël, B.P.Y., van den Broeke, M.R., 2018. Nonlinear rise in Greenland runoff in response to post-industrial Arctic warming. Nature 564 (7734), 104–108. https://doi.org/10.1038/s41586-018-0752-4.

Tsai, Y.L.S., Dietz, A., Oppelt, N., Kuenzer, C., 2019. Remote sensing of snow cover using spaceborne SAR: a review. Remote Sens. (Basel) 11 (12). https://doi.org/10.3390/rs11121456.

Wang, C., Deng, C., Wang, S., 2020. Imbalance-XGBoost: leveraging weighted and focal losses for binary label-imbalanced classification with XGBoost. Pattern Recogn. Lett. 136, 190–197. https://doi.org/10.1016/j.patrec.2020.05.035.

Wendleder, A., Gnatzy, G., Schmitt, A., Abdullahi, S.,2021. Evolution of supraglacial lakes on the Greenland Ice sheet. *Proceedings of the European Conference on Synthetic Aperture Radar, EUSAR*, *2021-March*, 527–530.

Wendleder, A., Schmitt, A., Erbertseder, T., D'Angelo, P., Mayer, C., Braun, M.H., 2021b. Seasonal evolution of supraglacial lakes on Baltoro Glacier from 2016 to 2020. Front. Earth Sci. 9 (December), 1–16. https://doi.org/10.3389/feart.2021.725394.

Yang, K., Smith, L., 2013. Supraglacial streams on the greenland ice sheet delineated from combined spectral-shape information in high-resolution satellite imagery. IEEE Geosci. Remote Sens. Lett. 10 (4), 801–805. https://doi.org/10.1109/LGRS.2012.2224316.

Yang, K., Smith, L.C., Cooper, M.G., Pitcher, L.H., Van As, D., Lu, Y., Lu, X., Li, M., 2021. Seasonal evolution of supraglacial lakes and rivers on the southwest Greenland Ice Sheet. J. Glaciol. 1–11. https://doi.org/10.1017/jog.2021.10.

Yuan, J., Chi, Z., Cheng, X., Zhang, T., Li, T., Chen, Z., 2020. Automatic extraction of Supraglacial lakes in Southwest Greenland during the 2014-2018 melt seasons based on convolutional neural network. Water (Switzerland) 12. https://doi.org/10.3390/w12030891.

Zheng, L., Li, L., Chen, Z., He, Y., Mo, L., Chen, D., Hu, Q., Wang, L., Liang, Q., Cheng, X., 2023. Multi-sensor imaging of winter buried lakes in the Greenland Ice Sheet. Remote Sens. Environ. 295 (May), 113688. https://doi.org/10.1016/j.rse.2023.113688.

Zhou, G., Cui, Y., Chen, Y., Yang, J., Rashvand, H., Yamaguchi, Y., 2011. Linear feature detection in polarimetric SAR images. IEEE Trans. Geosci. Remote Sens. 49 (4), 1453–1463. https://doi.org/10.1109/TGRS.2010.2081373.

Zhu, D., Zhou, C., Zhu, Y., Peng, B., 2022. Evolution of supraglacial lakes on Sermeq Avannarleq glacier, Greenland using Google Earth Engin. J. Hydrol.: Reg. Stud. 44, 101246. https://doi.org/10.1016/j.ejrh.2022.101246.

Zhu, D., Zhou, C., Zhu, Y., Wang, T., Zhang, C., 2023. *Monitoring of Supraglacial Lake Distribution and Full-Year Changes Using Multisource Time-Series Satellite Imagery*.

Zuo, Q., Chen, S., & Wang, Z., 2021. *R2AU-Net : Attention Recurrent Residual Convolutional Neural Network for Multimodal Medical Image Segmentation. 2021*. https://doi.org/10.1155/2021/6625688.